ACS APPLIED MATERIALS & INTERFACES

Research Article

www.acsami.org

Specific Detection and Simultaneously Localized Photothermal Treatment of Cancer Cells Using Layer-by-Layer Assembled Multifunctional Nanoparticles

Jianwei Shen, Kunyang Li, Liang Cheng,* Zhuang Liu, Shuit-Tong Lee, and Jian Liu*

Jiangsu Key Laboratory for Carbon-Based Functional Materials & Devices, Institute of Functional Nano & Soft Materials, Collaborative Innovation Center of Suzhou Nano Science and Technology, Soochow University, 199 Ren Ai Road, Suzhou Industrial Park, Suzhou, Jiangsu Province 215123, China

Supporting Information

ABSTRACT: There is a great need to develop multifunctional nanoparticles (MFNPs) for cancer biomarker-based detection and highly selective therapeutic treatment simultaneously. Here we describe a facile approach of layer-by-layer-assembled MFNPs conjugated with monoclonal antibody anti-HER2, demonstrating the specific detection of breast cancer BT474 cells (biomarker HER2 positive) with a high signal-to-noise ratio. The MFNPs contain a well-defined core–shell structure of UCNP@Fe_3O_4@Au coated by poly(ethylene glycol) (PEG) and anti-HER2 antibody, displaying excellent dispersity in various aqueous solutions. This unique combination of nanoparticles and ligand molecules allows us to perform photothermal treatment (PTT) of the cancer cells, while simultaneously quantifying the distribution of MFNPs on a cancer cell surface induced by antigen–antibody binding events. An important finding is that cancer cells adjacent to each other or in physical proximity within micrometers may end up with different fates of survival or death in PTT. This dramatic difference is determined by the antigen–antibody binding events at the interface of MFNPs and cells because of tumor cell heterogeneity. Therefore, our experiments reveal a new scale of the highly localized feature of the photothermal effect at the single–cell level illuminated by a continuous–wave near–IR laser.

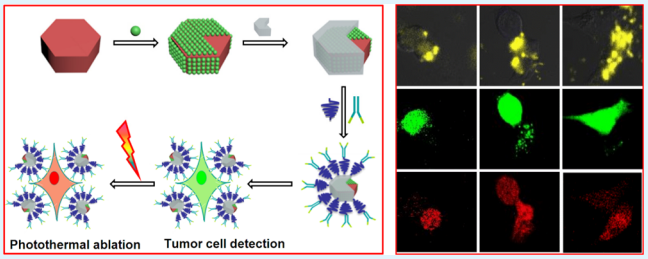

KEYWORDS: *detection of cancer cells, photothermal treatment, tumor heterogeneity, multifunctional nanoparticles, nano–bio interface*

INTRODUCTION

The battles against various cancers encourage revolutionary approaches, focusing on early diagnosis based on specific molecular features of diseases, improved therapy selection, and better methods of monitoring therapeutic outcomes with predictive power.[1,2] In response, theranostic nanomaterials have emerged combining both therapeutic agents and diagnostic imaging components into one package, with a potential to overcome otherwise undesirable differences in selectivity and biodistribution using separate agents in conventional techniques.[2−4] Theranostic nanoparticles promise selective administration of therapies simultaneously in situ where targeted cancer cells are detected, and continuous monitoring of therapeutic efficacy via the methods of molecular imaging. Therefore, there has been an increasing focus on the development of nanoparticle-based theranostics, driven by both the push of advances in nanotechnologies and the call for personalized medicine.[2−4] However, nanoparticle-based theranostics are still in their early stages of development; significant challenges remain to be addressed including strategic combination to fully utilize the featured performance of therapeutic and diagnostic components while minimizing their individual shortcomings.[2−4]

Photothermal treatment (PTT) enhanced by gold (Au) nanomaterials has been demonstrated as an effective approach for tumor ablation.[5−8] The feature of surface plasmon resonance (SPR) by Au nanomaterials enables ultrafast energy conversion of absorbed light into localized heat.[9,10] It also allows for a high efficiency of PTT at a much lower irradiation energy by laser because of the dramatic enhancement in the absorption cross section of Au nanoparticles (for example, 10^5 larger than that of indocyanine green dye molecules used in earlier demonstrations).[9] Conjugation of Au nanomaterials with ligands of small molecules,[11] aptamers or peptides,[12,13] and antibodies[6] has shown increased selectivity of targeting cancer cells with ablation while keeping the benign cells undamaged. On the other hand, various imaging applications using Au nanomaterials have been demonstrated in the literature,[6,14−17] including immunoelectron microscopy, dark-field microscopy, optical coherence tomography, reflectance confocal microscopy, photoacoustic tomography, and multiphoton plasmon resonance microscopy. The unique surface-enhanced Raman

Received: December 22, 2013
Accepted: April 2, 2014
Published: April 2, 2014

   dx.doi.org/10.1021/am405924g | ACS Appl. Mater. Interfaces 2014, 6, 6443−6452

resonance property of Au nanoparticles with the assistance of antibody bioconjugation has enabled targeting and spectroscopic detection of tumors in vivo.[18] In order to achieve desirable plasmonic or optical tunability, researchers have not only synthesized novel Au nanoparticles with characteristic shapes and sizes but also built a variety of composite nanostructures containing Au.[14,19,20] Nanoparticles containing a silica core and a thin Au shell with tunable ratios of core−shell thickness have been developed to cover a broader wavelength range of SPR from the visible-to-near-IR (NIR) region.[20] Fluorescent dyes or semiconductor quantum dots have been assembled to Au nanoparticles for potential multimodal imaging.[21−23] However, energy transfer between the fluorescent agents and Au nanoparticles has been demonstrated to be predominant. Thus, the undesired quenching effect of fluorescence by Au nanoparticles limits the bioimaging applications of these composite nanomaterials without using sophisticated strategies to address this challenge.[21−23]

Recently, we developed a layer-by-layer assembling technique to construct multifunctional nanoparticles (MFNPs).[24] These MFNPs were essentially composed of a Au nanoshell, superparamagnetic iron oxide nanoparticles in the intermediate layer, and rare-earth metal-doped fluorescent upconversion nanoparticles (UCNPs) in the core (UCNP@Fe_3O_4@Au). These MFNPs showed good performance in multimodal imaging assisted by the targeting ligand of a small molecule (folic acid).[24] Enrichment of MFNPs surrounding the tumor tissues induced by a magnetic force allowed the administration of PTT for tumor ablation with high efficacy.[25,26] Here we demonstrate that bioconjugation of the MFNPs with an anti-HER2 antibody (Scheme 1) enables the specific detection of HER2 positive cell lines such as breast cancer BT474, thus producing upconversion fluorescence signals with a high signal-to-noise ratio. Simultaneously, we are able to investigate PTT of cancer cells with MFNPs as prepared, revealing a highly localized feature of the photothermal effect at the single-cell level illuminated by a continuous-wave NIR laser. Our experiments show that the cells adjacent to each other or in physical proximity within micrometers may end up with different fates (survival or death) because of the inherent heterogeneity of cancer cells when under PTT. Compared with earlier demonstrations of the localized photothermal effect with a feature defined by the sizes of the laser spots,[5,7,24] our image data suggest a new scale of the featured resolution essentially determined by the antigen−antibody affinity binding events at the interface of MFNPs and cancer cells. Our work supports the idea that physical methods such as PTT enhanced by Au nanomaterials may convey dramatic advantages, namely, low side effects, because of this highly localized feature. However, a small percentage of surviving cancer cells may be left over from the isolated single therapeutic treatment because of the inherent heterogeneity of cancer cells. Therapies combining multibiomarker recognition or different treatment strategies with simultaneous image guidance will promise more effective solutions against cancers in the future.

Scheme 1. Schematic Illustration of the Synthesis Procedure of Anti-HER2-Conjugated MFNPs[a]

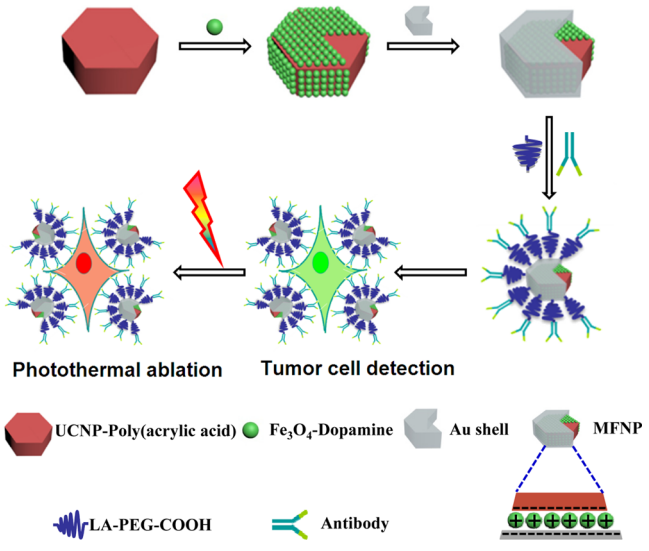

[a]Electrostatic interactions were employed for layer-by-layer assembling PAA-modified UCNP, dopamine-modified Fe_3O_4 NPs, and a Au shell (UCNP@Fe_3O_4@Au). MFNPs can find good applications in cancer cell detection and simultaneous PTT.

MATERIALS AND METHODS

Chemicals. All chemicals used in our experiment were analytical grade without further purification. $HAuCl_4$, Y_2O_3, Yb_2O_3, Er_2O_3, K_2CO_3, tetrahydrofuran, and NaOH were purchased from Shanghai Chemical Industrial Co. (Shanghai, China). The rare-earth trifluoroacetates were prepared by dissolving the rare-earth oxides in trifluoroacetic acid (CF_3COOH; Shanghai Chemical Industrial Co.). Tetrakis(hydroxymethyl)phosphonium chloride (80%), oleic acid (90%), oleylamine, 1-octadecene (>90%), benzyl ether (99%), 1,2-dexadecanediol (97%), diethylene glycol, $Fe(acac)_3$, formaldehyde, (±)-α-lipoic acid (LA), dopamine (DA), 1-ethyl-3-[3-(dimethylamino)propyl]carbodiimide (EDC), and *N*-hydroxysuccinimide (NHS) were purchased from Sigma-Aldrich.

Preparation of MFNPs with Layer-by-Layer Assembly. The components to assemble MFNPs were prepared by referring to previous reports.[24,27,28] The major steps included the preparation of Au seeds and a growth solution, synthesis of monodispersed Fe_3O_4 nanoparticles with superparamagnetic properties[27] modified with dopamine (DA), and synthesis of $NaYF_4$-based ($NaYF_4$: Yb, Er) UCNPs coated with poly(acrylic acid) (PAA).[24,28]

UCNP@Fe_3O_4 nanocomposites were synthesized by employing the technique of electrostatic assembly: DA-modified Fe_3O_4 nanoparticles (1 mg/mL) in water were slowly added into PAA−UCNP (1 mg/mL) after ultrasonication for 1 h. The mixture was treated by ultrasound for 30 min and then continuously stirred for 5 h. Excess Fe_3O_4 nanoparticles were removed by centrifugation at 6000 rpm and repeated water washing. The product displayed good dispersity in deionized (DI) water.

The outer Au nanoshells were assembled by attaching Au seeds on the surface of UCNP@Fe_3O_4 nanocomposites, followed by further growth of Au. A total of 1 mL of a UCNP@Fe_3O_4 solution (1 mg/mL UCNP) was mixed with 10 mL of a Au seed solution. After stirring for 4 h in room temperature, the unattached Au seeds were removed by centrifugation at 6000 rpm and repeated water washing. Afterward, 1 mL of a UCNP@Fe_3O_4 (0.1 mg/mL UCNP) solution (with Au seeds attached) was added with 10 μL of the aged Au growth solution with stirring. The reducing agent formaldehyde (29%) was then slowly introduced into the solution. LA−poly(ethylene glycol) (PEG)−COOH was synthesized in advance according to an established protocol.[24] The molecular weight of the PEG component was 5000. LA−PEG−COOH was added into the above mixture solution 30 min after the reaction of Au nanoshell growth was initiated. Excess reagents were removed by centrifugation at 12000 rpm for 10 min and repeated water washing.

After the steps above, MFNPs were successfully prepared, containing UCNP@Fe_3O_4@Au nanocomposites modified by LA−PEG−COOH on the surface (Scheme 1). MFNPs were stable in

aqueous solutions including DI water, a phosphate-buffered saline (PBS) buffer, or a cell culture medium.

Bioconjugation of an Anti-HER2 Antibody onto MFNPs. Bioconjugation of MFNPs was performed using a well-established technique of EDC−NHS covalent coupling. Anti-HER2 antibody was a product (Herceptin) of a monoclonal antibody from Roche Co., Ltd. Briefly, carboxylated MFNPs were dissolved in PBS (pH = 5.7) and stirred for 30 min. EDC and NHS (molar ratio of 1:1:2.5 NPs−EDC−NHS) were added simultaneously, and the mixture was stirred gently at room temperature for 1.5 h. The intermediate product of the coupling reaction was centrifuged (12000 rpm, 5 min) and washed with the PBS buffer (pH = 5.7) twice. Then the mixture was reacted with the anti-HER2 antibody (20 μL, 21 mg/mL) in PBS (pH = 7.4) for 4 h at 4 °C. The conjugated nanocomposites were collected by centrifugation (12000 rpm, 5 min) and washed with PBS (pH = 7.4) adequately. Anti-HER2-conjugated MFNPs were stored at 4 °C before the cell experiments.

Characterization of MFNPs. Scanning electron microscopy (SEM) images of these nanomaterials were acquired by using a FEI Quanta 200F scanning electron microscope. Transmission electron microscopy (TEM) and high-resolution TEM (HR-TEM) images were obtained using a Philips CM300 transmission electron microscope operating at an acceleration voltage of 200 kV. The phase and crystallography of the products were characterized by using a Shimadzu XRD-6000 X-ray diffractometer equipped with Cu Kα radiation (λ = 0.15406 nm). A scanning rate of 0.05°/s was applied to record the pattern in the 2θ range of 10−80°. The upconversion fluorescence spectra were obtained on a FluoroMax 4 luminescence spectrometer (HORIBA Jobin Yvon) with an external 980 nm laser diode (1 W, continuous wave with a 1 m optical fiber; Beijing Hi-Tech Optoelectronics Co., Ltd.) as the excitation source. UV/vis spectra were obtained with a PerkinElmer Lambda 750 UV/vis spectrophotometer. The size distribution and ζ potential were gained by using dynamic light scattering equipment (Zetasizer Nano ZS, ZEN3690, Malvern).

Cell Viability Assays, Cell Labeling, and Microscopy Imaging. The cell viability was measured using a standard methylthiazolyltetrazolium (MTT; Sigma-Aldrich) assay. HeLa and BT474 cancer cells were seeded into 96-well cell-culture plates at 5 × 10^4/well and then incubated with different concentrations of MFNPs for 24 h at 37 °C under 5% CO_2. The standard MTT assay was carried out to determine the cell viabilities relative to the untreated cells.

The reagents relevant to the cell culture were purchased from Invitrogen if no further specification is given. HeLa and BT474 cells obtained from the American Type Culture Collection were cultured in completed high-glucose Dulbecco's modified Eagle medium and RPMI-1640 cell medium, respectively, both supplemented with 10% fetal bovine serum (FBS) and 1% penicillin/streptomycin. The two cell lines were grown at 37 °C and 5% CO_2.

HeLa and BT474 cell lines were transferred, plated on glass coverslips (14 mm diameter), and maintained for adhesion for 24 h. Subsequently, after washing with PBS, the cells were incubated in a medium containing 200 μg/mL MFNP−antibody conjugates with or without FBS (we did not observe a difference) at 37 °C under 5% CO_2 for 1 or 2 h. Then the cell samples were sufficiently washed with PBS to remove excess nanoparticles. The cells were fixed with a 4% formaldehyde solution and stained with a 4′,6-diamidino-2-phenylindole (DAPI) solution. The experiments of upconversion luminescence (UCL) imaging in vitro were performed on a laser scanning confocal microscope (TCS SP5, Leica) with a customized laser (980 nm) upconversion luminescence setup. The laser device (980 nm) was adapted into the microscope as the excitation source for imaging with upconversion luminescence. The UCL emission of MFNPs from 500 to 560 nm was recorded by the microscope. The parameters of the setup were saved as a protocol for unifying the conditions of image acquisition.

PTT of BT474 and HeLa Cells Assisted by MFNP Conjugates. The BT474 and HeLa (the negative control cell line) cells were incubated with 250 μg/mL MFNP−antibody conjugates for 1 h at 4 °C. Additional negative control experiments were performed by various combinations of these factors, including choices of cell lines, with or without a laser, and with or without antibody-conjugated MFNPs. After excess MFNP−antibody conjugates were washed by the PBS buffer, the cell samples were incubated in the cell culture medium at 37 °C for another 2 h for cell recovery. Afterward, an 808 nm NIR laser was used to irradiate cells at a power density of 1 W/cm^2 for 5 min. After irradiation, we used calcein AM and propidium iodide (PI) to stain the cell samples. Multicolor images at the channels of calcein AM (500−530 nm), PI (600−660 nm), UCL (500−560 nm), and bright field were acquired using a customized laser confocal microscope.

Image Analysis. Multiple regions of interest (ROI) in the pool of acquired images were quantitatively analyzed for pixel intensities at the different channels of wavelengths. The criteria of selection included representative UCL labeling of the cells with differentiable recognition patterns and location proximity of neighboring cells to minimize the inhomogeneity of labeling conditions. Because we were particularly interested in the fate of the cells evading the recognition of anti-HER2-conjugated MFNPs during PTT, we allowed more ROI containing BT474 cells absent of UCL labeling in this selected group for further analysis. Therefore, the ratio of dead cells to living cells in this selected group did not represent the overall percentages of killed/surviving tumor cells in our typical photothermal experiment. With the help of an open-source software (*ImageJ*, a plug-in of cell outliner), we were able to locate the best fit of the individual cell boundary at different channels of the same stack of acquired images and then performed subsequent pixel analysis. We established a threshold to define the living or dead status of the individual cells by quantifying the ratio of pixel intensities at the channels of calcein AM and PI, respectively (AM/PI > 3, living cells; PI/AM > 3, dead cells). Then we attempted to calculate an index number reflecting the recognition events on each individual BT474 cell by the anti-HER2-conjugated MFNPs. The index was defined by the intensity-weighted pixels at the UCL channel over pixels of the total area of each individual cell. Briefly, an image of selected ROI was opened at the channel of UCL with the software *ImageJ* and then transferred to the 8-bit type. The total area and mean intensity at the UCL channel can be extracted by summing the pixels within the UCL boundaries (best fit). We set the minimal threshold of the pixel intensity larger than 10 to reduce background noise. All of the images of ROI were processed with identical settings. Pixels of the total area of each individual cell were obtained with a similar approach using the image channels of either calcein AM or PI. In summary, we repeated the experiments of PTT seven times. In these experiments, we scanned 243 different areas; 68 of those different areas were acquired with the objective 63×. There were 20−25 cells/image on average. Therefore, there were more than 1000 cells scanned at the high resolution (with the objective 63×). ROI containing 63 cells were chosen for detailed analysis because they met the criteria of selection for the study of the cell heterogeneity. These cells included 29 dead and 34 living BT474 cancer cells. Statistical analysis was performed using Microsoft Excel, including the standard unpaired *t* test with different variance.

RESULTS AND DISCUSSION

Preparation of Anti-HER2-Conjugated MFNPs. MFNPs, an abbreviation for the core−shell nanostructures of UCNP@Fe_3O_4@Au, were prepared using a layer-by-layer assembling approach (Scheme 1). UCNPs were synthesized by referencing an established procedure, consisting of Yb^{3+} and Er^{3+}-doped $NaYF_4$ nanoparticles (size distribution shown in Figure S1a in the Supporting Information, SI). Bright-green upconversion emission (with peak wavelengths of emission at 523 and 543 nm; Figure 2a) was produced when they were illuminated by an NIR (980 nm) laser. The surface of UCNPs was coated with PAA, thus enabling adsorption of positively charged Fe_3O_4 nanoparticles (6−9 nm; Figure S1b in the SI) with DA modification by electrostatic interaction. Then seed-induced reduction growth was employed to assemble a thin layer of Au

as the outer shell of the complex nanoparticles. The procedure of the above layer-by-layer assembly was monitored by UV/vis spectral measurements (Figure S1c in the SI). As-prepared MFNPs were further functionalized with LA−PEG−COOH to improve their dispersity in aqueous solutions. These MFNPs were available for bioconjugation with the anti-HER2 antibody by the well-established procedure of covalent linking between the carboxyl group (−COOH) and the amino group ($-NH_2$) using EDC and NHS.

Characterization of MFNP−Antibody Conjugates. Characterization of MFNPs was performed using SEM, TEM, and HR-TEM (Figure 1). The nanoparticles showed a uniform

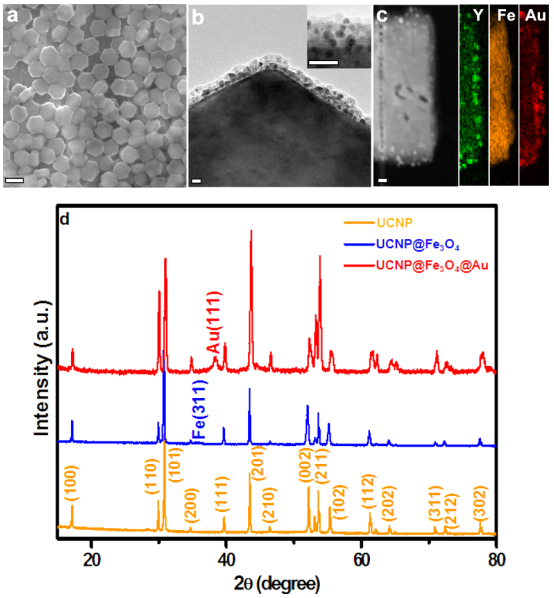

Figure 1. (a) SEM image of hexagonal MFNPs. Scale bar: 200 nm. (b) TEM image of MFNP at an acceleration voltage of 200 kV. The inset shows part of its corner with high resolution. Scale bar: 10 nm. (c) Scanning transmission electron microscopy image of part of MFNP. The mapping images show the elements of Y (green), Fe (orange), and Au (red). Scale bar: 10 nm. (d) XRD of UCNP, UCNP@Fe_3O_4, and UCNP@Fe_3O_4@Au with a scanning rate of 0.05°/s.

hexagonal shape, with a diameter of 200 nm on average (Figure 1a). It was also consistently confirmed by measurements using dynamic light scattering (Figure S3 in the SI). A distinct layer-by-layer structure was demonstrated, as shown in Figure 1b. The overall thickness of the Fe_3O_4 and Au layers was controlled well, approximately 20 nm (Figure 1b). Energy-dispersive X-ray (EDX) mapping (Figure 1c) and energy-dispersive spectroscopy (EDS) analysis (Figure S2 in the SI) were successfully employed to analyze the presence and distribution of yttrium (Y), iron (Fe), and Au elements in MFNPs and their ratios. The crystalline structure and composition of as-prepared UCNPs, UCNP@Fe_3O_4, and UCNP@Fe_3O_4@Au (MFNPs) were investigated using X-ray diffraction (XRD). As shown in Figure 1d, the positions of the characteristic peaks were well-correlated with the standard (JCPDS No. 028-1192). The diffraction peaks of the Fe and Au elements were successfully identified from the samples of MFNPs.

The previous studies indicated that Au played a significant role in quenching fluorescence during the preparation of composite nanomaterials. Therefore, in our design the intermediate layer of Fe_3O_4 was purposefully introduced as the buffer between the UCNP core and the Au shell in order to reduce the quenching effect on upconversion fluorescence. We compared the fluorescence of a series of intermediate and final products in solutions, including PAA-modified UCNP, UCNP@Fe_3O_4, UCNP@Fe_3O_4@Au (MFNPs), and UCNP@Au as an additional control. As shown in Figure 2a, in the geometry of UCNP@Au without a Fe_3O_4 buffer layer, the fluorescence of UCNPs was reduced because of the quenching effect of Au. This resulted in an intensity loss of nearly 90%, compared with the original UCNPs of identical concentration. In contrast, the fluorescence intensity showed considerable recovery (nearly 85% of the original UCNPs of identical concentration) because of incorporation of the buffer layer of Fe_3O_4 in the geometry of UCNP@Fe_3O_4@Au. This suggested that the additional distance of separation introduced by the buffer layer of Fe_3O_4 was important in reducing the energy-transfer efficiency of the undesired quenching phenomenon.[22]

PEGylation of MFNPs enhanced their dispersity in aqueous solutions. The carboxyl group as the terminal of PEGylation increased negative charges on the surface of MFNPs, thus minimizing aggregation of the nanoparticles. As shown in Figure S1d in the SI, MFNPs modified with LA−PEG−COOH possessed excellent stability (with a shelf life of 2−3 months) in different aqueous solutions including water, a PBS buffer solution, and the cell culture medium. Furthermore, the carboxyl group on the outer surface allowed bioconjugation of MFNPs with antibodies through coupling of the EDC and NHS covalent bond.

A series of ζ potentials were separately measured to monitor the preparation of nanoparticles at the different steps of synthesis or assembly. The changes of the ζ potentials were mostly distinct between adjacent steps, which indicated effective modification of the surface chemistry in each individual step. As shown in Figure 2b, we started with UCNPs modified by PAA, displaying a ζ potential of around −17.0 mV. It changed dramatically to +11.0 mV after the DA-coated Fe_3O_4 nanoparticles were assembled on the surface of UCNPs by electrostatic attractions. Then another remarkable change of the ζ potential occurred from +11.0 to −12.0 mV because of the assembly of Au shell as the new surface layer of MFNPs. The negative charges on the surface of MFNPs were increased by subsequent chemical modification with LA−PEG−COOH. At last, we observed a moderate change of the ζ potential from −16.2 to −6.5 mV, as the result of the reactive carboxyl group on MFNPs conjugated with the amino group of the anti-HER2 antibody by EDC−NHS coupling. As shown in Figure S3 in the SI, bioconjugation of MFNPs with the anti-HER2 antibody did not significantly change the size distribution of nanoparticles, suggesting that undesired aggregations of nanoparticles during the bioconjugation procedure were minimal. We attempted to further chemically characterize anti-HER2 antibody-conjugated MFNPs by element mapping of the EDX spectrum (Figure S4 in the SI). This successfully confirmed the composition of the elements of Fe and Au and the rare-earth metals including ytterbium (Yb), Y, and erbium (Er). The element of sulfur (S) was positively identified in the sample, derived from S-containing amino acids such as methionine, cystine, or dicystine in the antibody and/or LA. The presence of the nitrogen (N) element was attributed to the coating of dopamine and/or the amino acid residues of the antibody. In addition, we developed a new method to evaluate the performance of bioconjugation by using Coomassie Brilliant Blue G250, a dye widely used for

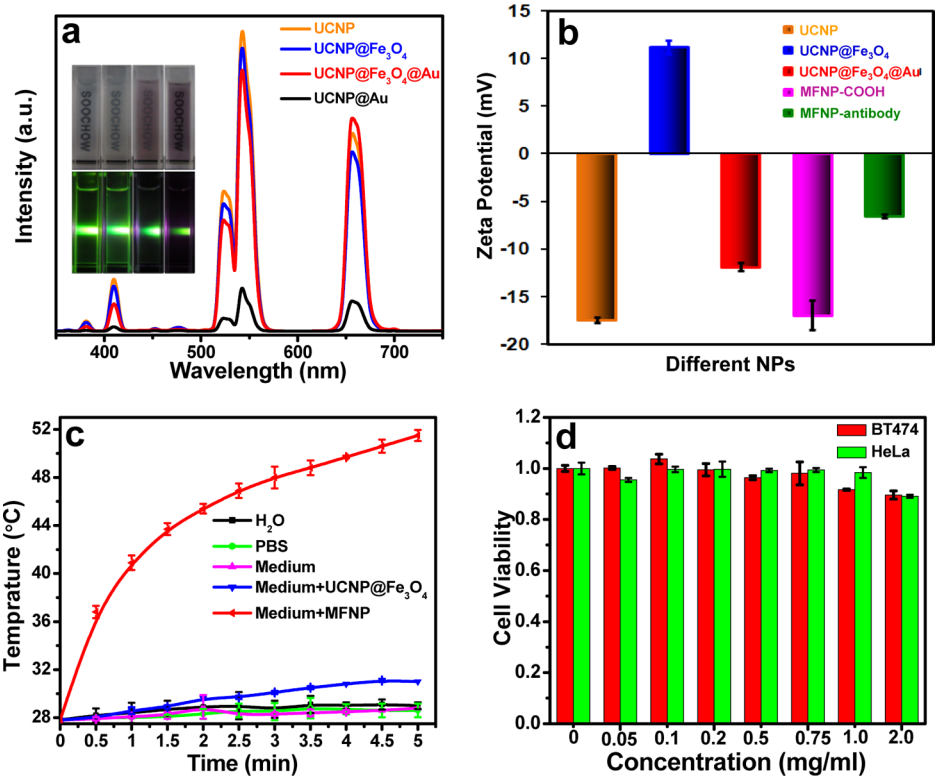

Figure 2. (a) Upconversion luminescence of the intermediate and final products of MFNPs, plus an additional control of UCNP@Au. The inset includes a panel of optical micrographs of these nanoparticles in aqueous solutions under ambient light (above) and a 980 nm laser (below). (b) ζ potential changes of the nanoparticles during synthesis. (c) Temperature changes of nanoparticles in solutions and blank controls illuminated by a 808 nm laser at a power density of 1 W/cm^2 for 5 min. (d) In vitro cytotoxicity MTT assays of two cell lines (BT474 and HeLa cells) incubated with various concentrations of MFNPs for 24 h, normalized by the cell samples without MFNP incubation (controls).

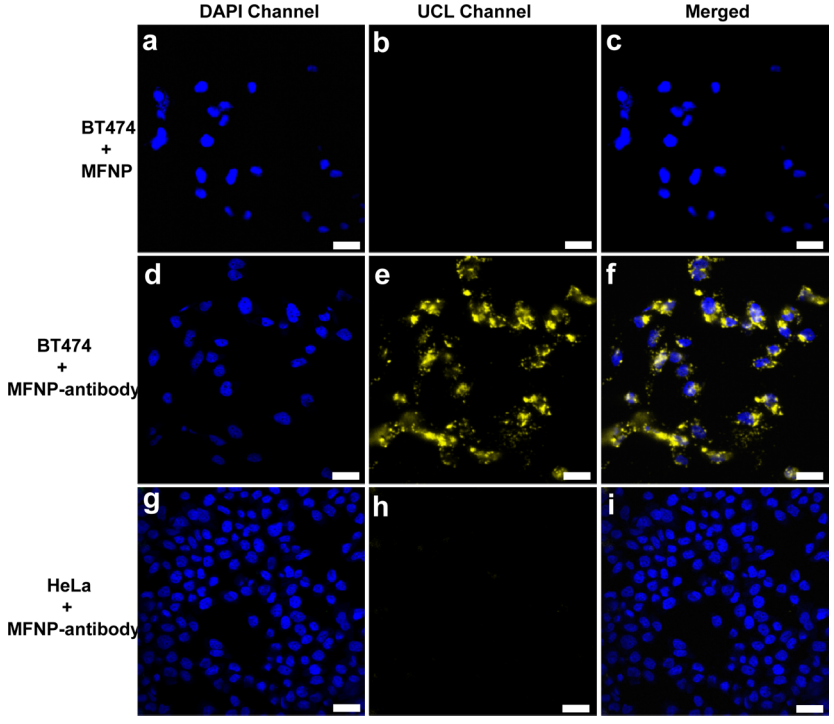

Figure 3. Fluorescent images of different cell lines incubated with the MFNPs as specified. The control experiments were performed with bare MFNPs without antibody conjugation and a HER2 negative cell line of HeLa. The images suggest specific recognition of HER2 positive BT474 cells with MFNP−antiHER2 conjugates: (a, d, and g) DAPI channel; (b, e, and h) UCL channel; (c, f, and i) merged. Excitation for MFNPs: 980 nm laser. Emission wavelength range for UCL acquisition: 500−560 nm. Objective: 63×. Scale bar: 25 μm.

dx.doi.org/10.1021/am405924g | ACS Appl. Mater. Interfaces 2014, 6, 6443−6452

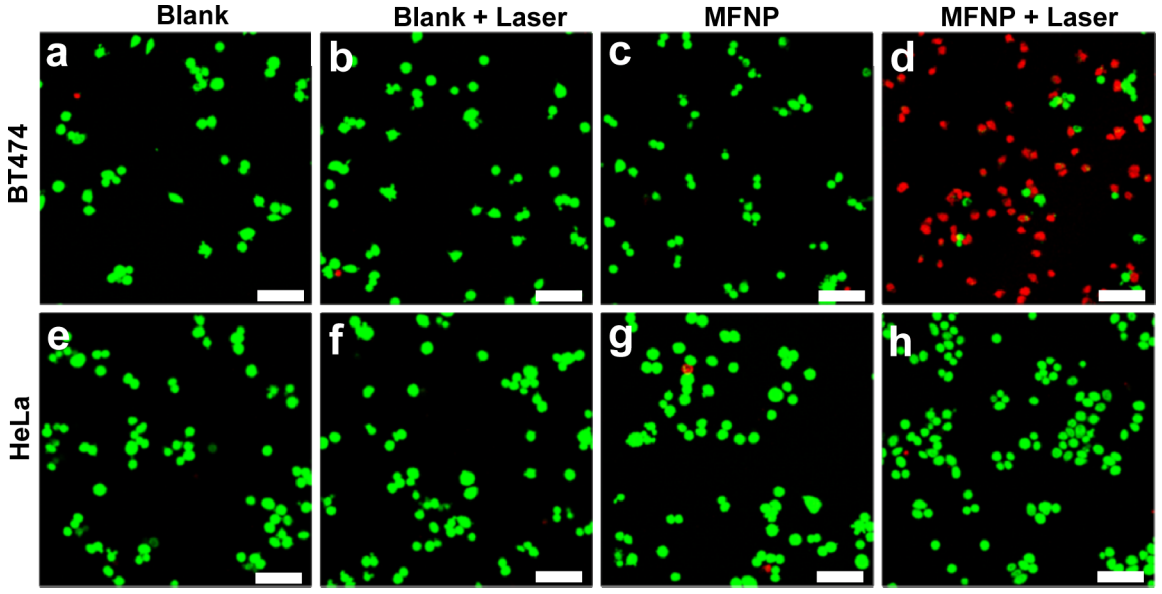

Figure 4. Images showing the living/dead status of cancer cells after PTT in the conditions as specified, including multiple control experiments. A costaining procedure was applied with the calcein AM (green, for living cells) and PI (red, for dead cells). Calcein AM: excitation, 488 nm laser; emission, 500−530 nm. PI: excitation, 488 nm laser; emission, 600−660 nm. UCL: excitation, 980 nm laser; emission, 500−560 nm. Objective: 10×. Scale bar: 100 μm.

protein detection. We performed the steps of washing and recollecting the MFNP−anti-HER2 many times so that unconjugated anti-HER2 molecules were removed completely (shown as supernatant+G250 in Figure S5 in the SI). There was a positive increase of the absorbance at 595 nm after the reaction of covalent coupling, suggesting successful bioconjugation of anti-HER2 on MFNPs.

Specific Detection of Tumor Cells with Antibody-Conjugated MFNPs. As-prepared anti-HER2-conjugated MFNPs were evaluated for tumor cell detection using the BT474 cell line as a positive model of the targeted tumor cells. The HER2 protein is a family member of the cell-membrane surface-bound tyrosine kinase receptors. Studies show that it is overexpressed in human breast cancer tissues and several other types of tumors. Therefore, HER2 has become an important biomarker in diagnosis and a valuable target of signaling pathways in the therapeutics of breast cancer. The BT474 cell line was originally isolated from an invasive ductal carcinoma of the breast overexpressing HER2. The HeLa cell line was included in our experiments as a negative control. The BT474 and HeLa cells were in parallel incubated with cell culture medium containing 200 μg/mL anti-HER2-conjugated MFNPs for 1 or 2 h. The cell samples were washed with PBS thoroughly and then stained by DNA intercalating fluorescent dye molecules DAPI for cell nuclear indication. The luminescence images of the cells were acquired using a confocal fluorescent microscope customized with an 980 nm NIR laser device. As shown in Figure 3, the sample of the HeLa cells displayed negligible fluorescence in the wavelength range between 500 and 560 nm under illumination by a 980 nm laser. In contrast, the BT474 cells exhibited intense upconversion luminescent signals in the identical wavelength range, resulting from the highly efficient affinity binding of anti-HER2−MFNP conjugates on the cell surface. In addition, another negative-control experiment was performed by incubating the BT474 cells with the bare MFNPs (surface modified with LA−PEG−COOH but without anti-HER2). The images showed negligible upconversion luminescence using bare MFNPs without anti-HER2 conjugation, supporting the observation that bare MFNPs lacked sufficient affinity binding on the target tumor cells (Figure 4a−c). Therefore, these results demonstrated that our approach enabled very specific detection of target tumor cells by antigen−antibody recognition, with a feature of a signal-to-noise ratio higher than 10 (Figure S6 in the SI). Upconversion luminescence has been well-known for its greatly reduced autofluorescence and low photodamage by NIR excitation.[24,28−32] In the literature, UCNPs conjugated with antibody or a small peptide of arginine−glycine−aspartic (RGD) have been applied for labeling cancer cells,[31,32] but simultaneous administration of PTT on the cancer cells recognized by the antibody has not been demonstrated yet.

Cytotoxicity of MFNPs in Vitro. The cytotoxicity of MFNPs was examined based on colorimetric measurement of the cellular enzymatic activity reducing the MTT dye (MTT assay). The cell samples of BT474 and HeLa were incubated with the culture medium containing a series of concentrations of MFNPs (in the range of 0−2 mg/mL) for 24 h. Then the enzyme activities of the cell samples were measured and normalized with the controls incubated without MFNPs. In the concentration of 0.2 mg/mL MFNPs (the concentration primarily used in our experiments), the cell samples remained more than 95% enzyme activity, which suggested very low cytotoxicity of MFNPs (Figure 2d). After the concentration of MFNPs was increased up to 2 mg/mL (10-fold higher than the primary concentration), the cell viabilities of these two cell lines were still nearly 90%. These measurements suggested that as-prepared MFNPs presented good biocompatibility, attributed to the well-controlled nanostructure of Au shell growth and subsequent PEGylation on the surface.

PTT of MFNP−Antibody Conjugates on the Tumor Cells. The photothermal effect of MFNP−antibody conjugates was investigated by a comparison of both the BT474 and HeLa cell samples. The samples of these two cell lines were incubated with anti-HER2-conjugated MFNPs for 1 h at 4 °C. The

incubation at low temperature reduced the energy-dependent endocytosis of nanoparticles by the cells. After washing with the PBS buffer and then recovery with the cell culture medium, the cell samples were irradiated by the NIR laser (808 nm) at a power density of 1 W/cm^2 for 5 min. In order to clarify the photothermal effect of anti-HER2-conjugated MFNPs, we included the control experiments of examining different combinations of multiple factors such as positive and negative cell lines, administration or not of MFNP−antibody conjugates, and with or without 808 laser illumination. As shown in Figure 4, the combination of anti-HER2-conjugated MFNPs and laser illumination demonstrated a significant photothermal killing effect on the target tumor cells of BT474. The staining pattern with the living/dead cell dye molecules (calcein AM and PI) clearly showed that the majority of BT474 cells were killed by this combination, therefore producing the prevalent signals (red) by the dye molecules of PI for the dead cells. In contrast, the other combinations cannot kill the tumor cells efficiently because at least one necessary factor for the photothermal effect was absent. In these cases, the cell samples predominantly displayed the signals (green) by the dye molecules of calcein AM for living cells. In these negative control experiments, occasionally there were a few cells showing the signals of red by the stain of PI. Even though it might suggest that the cells were dead, the reason for the cell death was unlikely to derive from the photothermal effect because overall the staining pattern dramatically differed from the images of the positive experiment (Figure 4d).

We further measured the temperature changes of the cell culture medium containing MFNPs and its analogue (UCNP@Fe_3O_4 without the Au shell) under irradiation of a 808 nm laser. As shown in Figure 2c, the medium solution containing MFNPs appeared to be responsive to NIR laser illumination with a rapid temperature increase (from 27.8 to 51.2 °C in 5 min). In the control experiments in parallel, the medium solution containing nanoparticles lacking a Au shell (the analogue) or other blank buffer solutions displayed much slower temperature growth (smaller than 3 °C change in 5 min) with identical illumination. Therefore, this suggested that the Au nanoshell in as-prepared MFNPs played an important role for introducing rapid photothermal energy conversion. However, these experiments were performed in the bulky solutions containing nanoparticles. The local temperature change at the nanoscale near the nanoparticle surface had not been determined yet but was expected to be more dramatic than the result of the measurements at the macroscale using bulky solutions.[33,34] Thermally and subsequent mechanically induced damages on the cell membrane integrity were proposed as a leading cause of tumor cell death suffered from PTT.[8,35] Interestingly, previous studies showed that internalization of Au nanorods actually reduced the efficiency of photothermal ablation of tumor cells.[35] Aggregation of Au nanomaterials on the tumor cell surface may amplify the damage to the membrane integrity. These raised our interest in further investigating the localized feature of PTT on the tumor cells.

Localized Photothermal Feature Defined by the Affinity Binding Events of Biomolecules. The localized feature of PTT has previously been investigated using Au nanoparticles, Au nanorods, or Au nanocomposites.[5−8,24] In those experiments, manually selected areas in the cell culture incubated with various Au nanomaterials were irradiated with a laser for administration of PTT, producing living/dead cell patterns defined by the sizes of laser spots at the scale of millimeters.[5,7,24] Here we further demonstrated that PTT was highly localized at the resolution of individual cells essentially determined by the affinity binding events of antigen−antibody interactions.

In our experiments of PTT of BT474 tumor cells with anti-HER2−MFNP conjugates, a portion of the BT474 cells appeared to evade PTT. We repeated the experiments and found that there were 5−25% BT474 cells reproducibly surviving PTT by NIR laser irradiation (Figure 4d). In addition, we performed MTT assays after PPT for the purpose of quantification. As shown in Figure S7 in the SI, the viability of the BT474 cells was reduced significantly after incubation with anti-HER2-conjugated MFNPs and subsequent PTT. Given the good biocompatibility of our nanoparticles (Figure 2d), this supported the effectiveness of our approach in PTT. BT474 cells lost most but not 100% cell viability in the condition of 0.25 mg/mL MFNP−anti-HER2 and PTT, consistent with the results by fluorescent cell imaging. Indeed, the previous studies from the literature also suggested a similar phenomenon of the tumor cells enduring PTT.[5,7] However, most of the experiments in the literature did not provide further knowledge regarding the occurrence of this phenomenon because of the limitation of their materials or methods.

Using MFNP−antibody conjugates, we were able to acquire stacks of images containing the wavelength channels for calcein AM and PI and the channel of upconversion luminescence excited by the NIR laser, which was far from the excitation source of the former two fluorescent dyes. Therefore, our approach was featured with high image quality with low noise or signal contamination, facilitating our studies of the distribution of MFNP−antibody conjugates on the tumor cell surface and the effectiveness of PTT simultaneously. The images suggested that the photothermal effect of killing tumor cells correlated well with the amounts and distribution of MFNP−antibody conjugates on the cells (Figure 5a,b). We developed a method of image analysis to semiquantitatively measure the amounts of MFNP−antibody conjugate labeling on the cell surface induced by antigen−antibody recognition. The upconversion fluorescent pixels of MFNPs weighted by the intensity were normalized with pixels of the total area of each individual cell, producing a numerical index of the amounts of MFNP binding on the cell surface. In the meantime, the fluorescence signal ratio of calcein AM and PI staining was utilized to define the living/dead status of the same cell individually (Figure 6). We deliberately selected the ROI containing the cells adjacent to each other or separated with only micrometers for analysis. In such physical proximity, the inhomogeneity of labeling conditions such as fluctuation of MFNP concentrations in the medium was minimized; thus, the abundance of the biomarker (HER2 antigen) on the surface of individual cells dominated the affinity binding events between the antigen and antibody interactions. As shown in Figure 5c, the numerical index of the cells killed by PTT was nearly five-fold higher than that of the cells evading identical treatment, suggesting that photothermal ablation of tumor cells required sufficient antigen−antibody recognition events. Furthermore, multiple images (Figure 5b) revealed that the BT474 tumor cells adjacent to each other may end up with totally different fates (living or dead). The difference of their fates correlated well with the distinct distribution pattern and amounts of anti-HER2-conjugated MFNPs on these cells. These results indicated a highly localized feature of PTT at the resolution

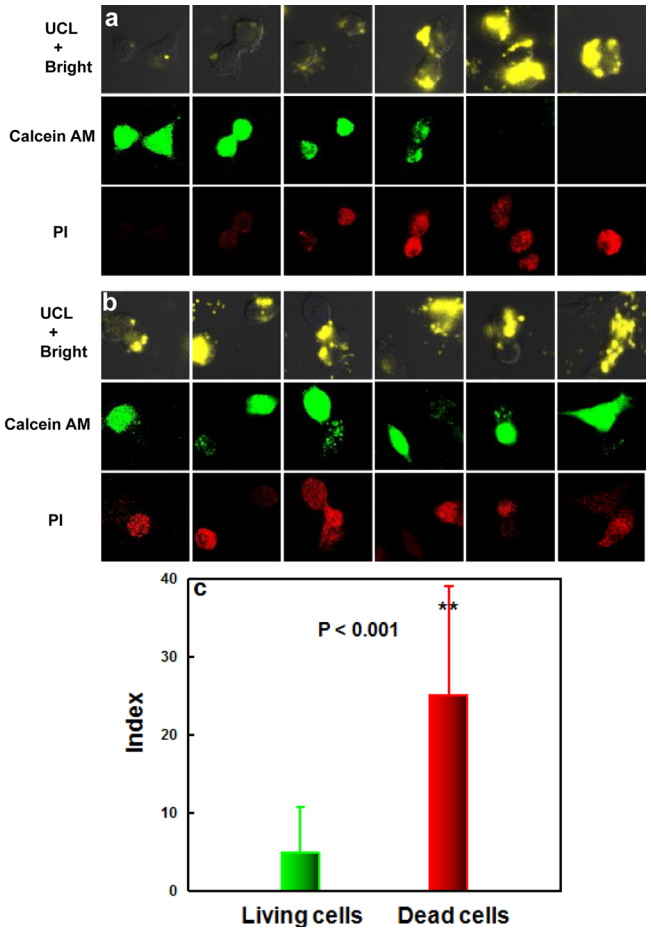

Figure 5. (a and b) Different fates of the cells adjacent to each other or in physical proximity after PTT. In each panel, three images arranged in a column were acquired from the same region but in the separate channels as specified. Objective: 63×. (c) Statistical analysis of the individual cells, suggesting that the amounts of anti-HER2-conjugated MFNPs on the cell surface of the living and dead cells are significantly different. 63 cells were analyzed, including 29 dead and 34 living BT474 cancer cells. *p* value: <0.001 in a standard unpaired *t* test. Error bar: standard deviation.

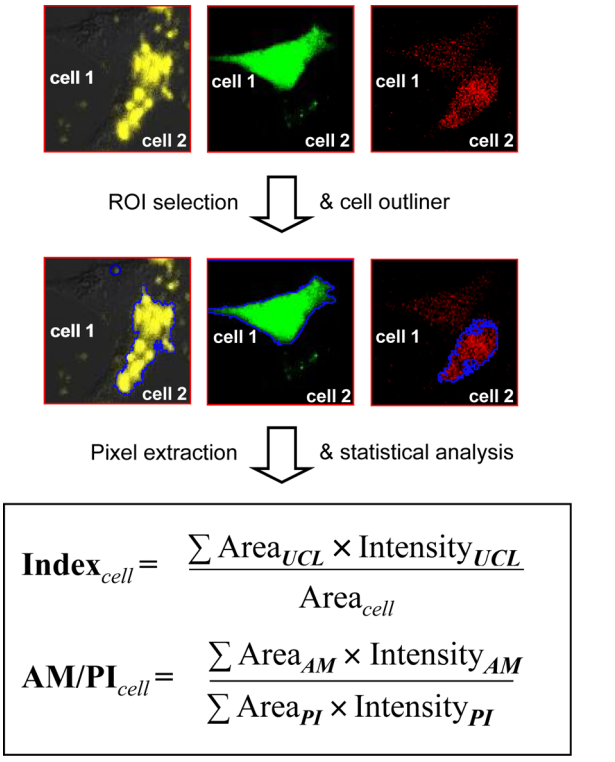

Figure 6. Schematic illustration of the image analysis procedure of the ROI containing cells adjacent to each other but with distinct cellular fates after PTT.

of individual cells. Otherwise, the cells that were not sufficiently recognized by the antibody-conjugated MFNPs but were adjacent to the other cells mounting with aggregation of MFNPs could not survive PTT (Figure 5b). This scale of the localized feature at the single-cell level in our approach was essentially determined by the antigen−antibody binding events at the interface of MFNPs and cancer cells. Therefore, it was distinctively different from the previously observed resolution of the photothermal effect, which was typically in the size of a laser spot (millimeters) using a manual method to determine the boundary of the living/dead cells. The new evidence of this highly localized feature by our approach will foster the development of PTT with a performance of minimal invasiveness in practical applications.

It was also noticeable that PTT alone could not kill all of the cancer cells. Cancer cells are notorious for their complicated heterogeneity (at multiple levels) in genetic and protein expression, which contributes to their amazing ability to resist various therapeutic treatments and subsequent reoccurrence.[36−38] Technical advances in single-cell gene expression profiling and sequencing revealed a predominant heterogeneity of transcription activity for the cell population.[39,40] The cell numbers versus the transcript levels of the genes from single cells fitted log-normal distribution, covering a range of mRNA differences of more than 2 orders of magnitude.[41] Assisted by microfluidic technology, researchers were able to quantify the absolute copy numbers of mRNAs sensitively at the single-cell level.[42] They found that a noticeable percentage of cells did not express the biomarker genes in a detectable level, which would be missed in a conventional bulk analysis using a population of cells.[42] A similar scope of cell population heterogeneity in gene expression was supported by other studies but also correlated to heterogeneous functions of the cells.[43] The complicated heterogeneity derived from a number of factors including, at least but not last, various stages of the cell cycle, differentiation in subtle ways, and changes of RNA processing stimulated by environmental fluctuations. A consequence of heterogeneity appeared to be survival of tumor cells and development of the resistance to therapeutic treatment. Therefore, the inherent heterogeneity of tumor cells provided a clue to the result of our experiments, explaining that a small portion of BT474 cells were not recognized by the anti-HER2-conjugated MFNPs and subsequently evaded PTT. Our experiments indicated that isolated therapeutic treatment based on a single biomarker might miss a portion of the tumor cells undergoing stochastic changes of biomolecules. It is of profound importance and favorably suggests that the development of combinatorial therapies enhanced by multibiomarker recognition[44] is in great need to address the challenge of tumor heterogeneity.

CONCLUSIONS

We have developed anti-HER2-conjugated MFNPs with a core−shell structure of UCNP@Fe_3O_4@Au using the layer-by-

layer assembling approach. We have demonstrated that these bioconjugated MFNPs can detect breast cancer BT474 cells (HER2+) with high specificity, producing upconversion luminescence with a high signal-to-noise ratio. Using these MFNPs, we are able to perform PTT on the targeted cancer cells and simultaneously quantify the distribution of MFNPs on the cell surface induced by antigen−antibody binding events. Our image data have revealed that the cells adjacent to each other or in physical proximity within micrometers may turn out to have totally different cellular fates (survival or death) after PTT, derived from the inherent heterogeneity of cancer cells. Therefore, our experiments suggest a highly localized feature of the photothermal effect at the single-cell level illuminated by a continuous-wave NIR laser. We believe that combinatorial therapeutic treatments, assisted by simultaneous imaging guidance, will play an increasingly important role in addressing cancer therapies in the future.

■ ASSOCIATED CONTENT

Ⓢ Supporting Information

Size distribution of UCNP, Fe_3O_4, MFNPs, and anti-HER2-conjugated MFNPs, UV/vis spectra of the nanoparticles, optical micrographs of MFNPs in various aqueous solutions, EDS analysis and EDX spectrum, UV/vis spectra of MFNP, MFNP+G250, MFNP−anti-HER2+G250, and supernatant +G250, MTT assays after PTT, and analysis of the signal-to-noise ratio. This material is available free of charge via the Internet at http://pubs.acs.org.

■ AUTHOR INFORMATION

Corresponding Authors

*E-mail: jliu@suda.edu.cn. Tel: 0512 65884565 Fax: 0512 65880820.

*E-mail: lcheng2@suda.edu.cn. Tel: 0512 65884565. Fax: 0512 65880820.

Notes

The authors declare no competing financial interest.

■ ACKNOWLEDGMENTS

This work was supported by the Major State Basic Research Development Program (Grants 2013CB932702 and 2012CB932601) and by the National Natural Science Foundation of China (Grants 21275106 and 51302180), a project supported by the Priority Academic Program Development of Jiangsu Higher Education Institutions and Doctoral Fund of Ministry of Education of China (Grant 20123201120025). J.L. was supported by the "Youth 1000-plan" in the Recruitment Program of Global Experts. We thank Marcella Crawford for her kind help in revising this manuscript.

■ REFERENCES

(1) Cole, A. J.; Yang, V. C.; David, A. E. Cancer Theranostics: The Rise of Targeted Magnetic Nanoparticles. *Trends Biotechnol.* **2011**, *29*, 323−332.

(2) Xie, J.; Lee, S.; Chen, X. Nanoparticle-based Theranostic Agents. *Adv. Drug Delivery Rev.* **2010**, *62*, 1064−1079.

(3) Lee, D. Y.; Li, K. C. P. Molecular Theranostics: A Primer for the Imaging Professional. *Am. Roentgen Ray Soc.* **2011**, *197*, 318−324.

(4) Kelkar, S. S.; Reineke, T. M. Theranostics: Combining Imaging and Therapy. *Bioconjugate Chem.* **2011**, *22*, 1879−1903.

(5) Loo, C.; Lowery, A.; Halas, N.; West, J.; Drezek, R. Immunotargeted Nanoshells for Integrated Cancer Imaging and Therapy. *Nano Lett.* **2005**, *5*, 709−711.

(6) Huang, X.; El-Sayed, I. H.; Qian, W.; El-Sayed, M. A. Cancer Cell Imaging and Photothermal Therapy in the Near-Infrared Region by Using Gold Nanorods. *J. Am. Chem. Soc.* **2006**, *128*, 2115−2120.

(7) Au, L.; Zheng, D.; Zhou, F.; Li, Z.-Y.; Li, X.; Xia, Y. A Quantitative Study on the Photothermal Effect of Immuno Gold Nanocages Targeted to Breast Cancer Cells. *ACS Nano* **2008**, *2*, 1645−1652.

(8) Wang, S.; Chen, K.-J.; Wu, T.-H.; Wang, H.; Lin, W.-Y.; Ohashi, M.; Chiou, P.-Y.; Tseng, H.-R. Photothermal Effects of Supramolecularly Assembled Gold Nanoparticles for the Targeted Treatment of Cancer Cells. *Angew. Chem., Int. Ed.* **2010**, *49*, 3777−3781.

(9) Jain, P. K.; El-Sayed, I. H.; El-Sayed, M. A. Au Nanoparticles Target Cancer. *Nano Today* **2007**, *2*, 18−29.

(10) Berciaud, S.; Cognet, L.; Blab, G. A.; Lounis, B. Photothermal Heterodyne Imaging of Individual Nonfluorescent Nanoclusters and Nanocrystals. *Phys. Rev. Lett.* **2004**, *93*, 257402.

(11) Bhattacharya, R.; Patra, C. R.; Earl, A.; Wang, S.; Katarya, A.; Lu, L.; Kizhakkedathu, J. N.; Yaszemski, M. J.; Greipp, P. R.; Mukhopadhyay, D.; Mukherjee, P. Attaching Folic Acid on Gold Nanoparticles Using Noncovalent Interaction via Different Polyethylene Glycol Backbones and Targeting of Cancer Cells. *Nanomed.: Nanotechnol., Biol., Med.* **2007**, *3*, 224−238.

(12) Kim, D.; Jeong, Y. Y.; Jon, S. A Drug-loaded Aptamer-gold Nanoparticle Bioconjugate for Combined CT Imaging and Therapy of Prostate Cancer. *ACS Nano* **2010**, *4*, 3689−3696.

(13) Li, Z.; Huang, P.; Zhang, X.; Lin, J.; Yang, S.; Liu, B.; Gao, F.; Xi, P.; Ren, Q.; Cui, D. RGD-conjugated Dendrimer-modified Gold Nanorods for In Vivo Tumor Targeting and Photothermal Therapy. *Mol. Pharmacol.* **2010**, *7*, 94−104.

(14) Cobley, C. M.; Chen, J.; Cho, E. C.; Wang, L. V.; Xia, Y. Gold Nanostructures: A Class of Multifunctional Materials for Biomedical Applications. *Chem. Soc. Rev.* **2011**, *40*, 44−56.

(15) Daniel, M.-C.; Astruc, D. Gold Nanoparticles: Assembly, Supramolecular Chemistry, Quantum-Size-Related Properties, and Applications toward Biology, Catalysis, and Nanotechnology. *Chem. Rev.* **2003**, *104*, 293−346.

(16) Chen, J.; Saeki, F.; Wiley, B. J.; Cang, H.; Cobb, M. J.; Li, Z. Y.; Au, L.; Zhang, H.; Kimmey, M. B.; Li, X.; Xia, Y. Gold Nanocages: Bioconjugation and Their Potential Use as Optical Imaging Contrast Agents. *Nano Lett.* **2005**, *5*, 473−477.

(17) Yang, X.; Skrabalak, S. E.; Li, Z.-Y.; Xia, Y.; Wang, L. V. Photoacoustic Tomography of a Rat Cerebral Cortex in vivo with Au Nanocages as an Optical Contrast Agent. *Nano Lett.* **2007**, *7*, 3798−3802.

(18) Qian, X.; Peng, X.-H.; Ansari, D. O.; Yin-Goen, Q.; Chen, G. Z.; Shin, D. M.; Yang, L.; Young, A. N.; Wang, M. D.; Nie, S. In Vivo Tumor Targeting and Spectroscopic Detection with Surface-enhanced Raman Nanoparticle Tags. *Nat. Biotechnol.* **2008**, *26*, 83−90.

(19) Personick, M. L.; Langille, M. R.; Wu, J.; Mirkin, C. A. Synthesis of Gold Hexagonal Bipyramids Directed by Planar-Twinned Silver Triangular Nanoprisms. *J. Am. Chem. Soc.* **2013**, *135*, 3800−3803.

(20) Loo, C.; Lin, A.; Hirsch, L.; Lee, M.-H.; Barton, J.; Halas, N.; West, J.; Drezek, R. Nanoshell-Enabled Photonics-Based Imaging and Therapy of Cancer. *Technol. Cancer Res.* **2004**, *3*, 33−40.

(21) Nitin, N.; Javier, D. J.; Richards-Kortum, R. Oligonucleotide-Coated Metallic Nanoparticles as a Flexible Platform for Molecular Imaging Agents. *Bioconjugate Chem.* **2007**, *18*, 2090−2096.

(22) Jin, Y.; Gao, X. Plasmonic Fluorescent Quantum Dots. *Nat. Nano* **2009**, *4*, 571−576.

(23) Shevchenko, E. V.; Ringler, M.; Schwemer, A.; Talapin, D. V.; Klar, T. A.; Rogach, A. L.; Feldmann, J.; Alivisatos, A. P. Self-Assembled Binary Superlattices of CdSe and Au Nanocrystals and Their Fluorescence Properties. *J. Am. Chem. Soc.* **2008**, *130*, 3274−3275.

(24) Cheng, L.; Yang, K.; Li, Y.; Chen, J.; Wang, C.; Shao, M.; Lee, S.-T.; Liu, Z. Facile Preparation of Multifunctional Upconversion Nanoprobes for Multimodal Imaging and Dual-Targeted Photothermal Therapy. *Angew. Chem., Int. Ed.* **2011**, *50*, 7385−7390.

(25) Cheng, L.; Yang, K.; Li, Y.; Zeng, X.; Shao, M.; Lee, S.-T.; Liu, Z. Multifunctional Nanoparticles for Upconversion Luminescence/MR Multimodal Imaging and Magnetically Targeted Photothermal Therapy. *Biomaterials* **2012**, *33*, 2215−2222.
(26) Wang, C.; Cheng, L.; Xu, H.; Liu, Z. Towards Whole-body Imaging at The Single Cell Level Using Ultra-sensitive Stem Cell Labeling with Oligo-arginine Modified Upconversion Nanoparticles. *Biomaterials* **2012**, *33*, 4872−4881.
(27) Sun, S.; Zeng, H.; Robinson, D. B.; Raoux, S.; Rice, P. M.; Wang, S. X.; Li, G. Monodisperse MFe2O4 (M = Fe, Co, Mn) Nanoparticles. *J. Am. Chem. Soc.* **2003**, *126*, 273−279.
(28) Mai, H.-X.; Zhang, Y.-W.; Si, R.; Yan, Z.-G.; Sun, L.-d.; You, L.-P.; Yan, C.-H. High-Quality Sodium Rare-Earth Fluoride Nanocrystals: Controlled Synthesis and Optical Properties. *J. Am. Chem. Soc.* **2006**, *128*, 6426−6436.
(29) Wang, F.; Deng, R.; Wang, J.; Wang, Q.; Han, Y.; Zhu, H.; Chen, X.; Liu, X. Tuning Upconversion Through Energy Migration in Core−shell Nanoparticles. *Nat. Mater.* **2011**, *10*, 968−973.
(30) Xing, H.; Bu, W.; Zhang, S.; Zheng, X.; Li, M.; Chen, F.; He, Q.; Zhou, L.; Peng, W.; Hua, Y.; Shi, J. Multifunctional Nanoprobes for Upconversion Fluorescence, MR and CT Trimodal Imaging. *Biomaterials* **2012**, *33*, 1079−1089.
(31) Wang, M.; Mi, C.-C.; Wang, W.-X.; Liu, C.-H.; Wu, Y.-F.; Xu, Z.-R.; Mao, C.-B.; Xu, S.-K. Immunolabeling and NIR-Excited Fluorescent Imaging of HeLa Cells by Using $NaYF_4$:Yb,Er Upconversion Nanoparticles. *ACS Nano* **2009**, *3*, 1580−1586.
(32) Xiong, L.; Chen, Z.; Tian, Q.; Cao, T.; Xu, C.; Li, F. High Contrast Upconversion Luminescence Targeted Imaging in Vivo Using Peptide-Labeled Nanophosphors. *Anal. Chem.* **2009**, *81*, 8687−8694.
(33) Cognet, L.; Tardin, C.; Boyer, D.; Choquet, D.; Tamarat, P.; Lounis, B. Single Metallic Nanoparticle Imaging for Protein Detection in Cells. *Proc. Natl. Acad. Sci. U.S.A.* **2003**, *100*, 11350−11355.
(34) Dias, J. T.; Moros, M.; del Pino, P.; Rivera, S.; Grazú, V.; de la Fuente, J. M. DNA as a Molecular Local Thermal Probe for the Analysis of Magnetic Hyperthermia. *Angew. Chem., Int. Ed.* **2013**, *125*, 11740−11743.
(35) Tong, L.; Zhao, Y.; Huff, T. B.; Hansen, M. N.; Wei, A.; Cheng, J. X. Gold Nanorods Mediate Tumor Cell Death by Compromising Membrane Integrity. *Adv. Mater.* **2007**, *19*, 3136−3141.
(36) Pece, S.; Tosoni, D.; Confalonieri, S.; Mazzarol, G.; Vecchi, M.; Ronzoni, S.; Bernard, L.; Viale, G.; Pelicci, P. G.; Fiore, P. P. D. Biological and Molecular Heterogeneity of Breast Cancers Correlates with Their Cancer Stem Cell Content. *Cell* **2009**, *140*, 62−73.
(37) Shipitsin, M.; Campbell, L. L.; Argani, P.; Weremowicz, S.; Bloushtain-Qimron, N.; Yao, J.; Nikolskaya, T.; Serebryiskaya, T.; Beroukhim, R.; Hu, M.; Halushka, M. K.; Sukumar, S.; Parker, L. M.; Anderson, K. S.; Harris, L. N.; Garber, J. E.; Richardson, A. L.; Schnitt, S. J.; Nikolsky, Y.; Gelman, R. S.; Polyak, K. Molecular Definition of Breast Tumor Heterogeneity. *Cancer Cell* **2007**, *11*, 259−273.
(38) Liu, J.; Lau, S. K.; Varma, V. A.; Moffitt, R. A.; Caldwell, M.; Liu, T.; Young, A. N.; Petros, J. A.; Osunkoya, A. O.; Krogstad, T.; Leyland-Jones, B.; Wang, M. D.; Nie, S. Molecular Mapping of Tumor Heterogeneity on Clinical Tissue Specimens with Multiplexed Quantum Dots. *ACS Nano* **2010**, *4*, 2755−2765.
(39) Levsky, J. M.; Shenoy, S. M.; Pezo, R. C.; Singer, R. Single-Cell Gene Expression Profiling. *Science* **2002**, *297*, 836−840.
(40) Navin, N.; Kendall, J.; Troge, J.; Andrews, P.; Rodgers, L.; McIndoo, J.; Cook, K.; Stepansky, A.; Levy, D.; Esposito, D.; Muthuswamy, L.; Krasnitz, A.; McCombie, W. R.; Hicks, J.; Wigler, M. Tumour Evolution Inferred by Single-cell Sequencing. *Nature* **2011**, *472*, 90−94.
(41) Bengtsson, M.; Ståhlberg, A.; Rorsman, P.; Kubista, M. Gene Expression Profiling in Single Cells from The Pancreatic Islets of Langerhans Reveals Lognormal Distribution of mRNA Levels. *Genome Res.* **2005**, *15*, 1388−1392.
(42) Zhong, J. F.; Chen, Y.; Marcus, J. S.; Scherer, A.; Quake, S. R.; Taylorb, C. R.; Weinera, L. P. A Microfluidic Processor for Gene Expression Profiling of Single Human Embryonic Stem Cells. *Lab Chip* **2008**, *8*, 68−74.
(43) Tan, D. W. M.; Jensen, K. B.; Trotter, M. W. B.; Connelly, J. T.; Broad, S.; Watt, F. M. Single-cell Gene Expression Profiling Reveals Functional Heterogeneity of Undifferentiated Human Epidermal Cells. *Neural Dev. Stem Cells* **2013**, *140*, 1433−1444.
(44) Wu, C.-H.; Huang, Y.-Y.; Chen, P.; Hoshino, K.; Liu, H.; Frenkel, E. P.; Zhang, J. X. J.; Sokolov, K. V. Versatile Immunomagnetic Nanocarrier Platform for Capturing Cancer Cells. *ACS Nano* **2013**, *7*, 8816−8823.